






 Cite this: *Lab Chip*, 2019, 19, 2598

Polymeric microfluidic continuous flow mixer combined with hyperspectral FT-IR imaging for studying rapid biomolecular events†

 Hyukjin Jang, ^{ac} Ashtamurthy S. Pawate, ^b
Rohit Bhargava ^{*abc} and Paul J. A. Kenis ^{*abc}

Early reaction intermediates in protein folding, such as those resulting in β -amyloid formation due to transient misfolding, emerge within a few hundred microseconds. Here, we report a method to obtain sub-millisecond temporal resolution and molecular structural information of protein (mis-)folding events by using a microfluidic continuous-flow mixer (MCFM) in combination with Fourier transform infrared (FT-IR) imaging. The MCFMs are made out of cyclic olefin copolymer (COC) films, because this approach allows for rapid prototyping of different mixer designs. Furthermore, COC offers high IR transparency between 1500 and 2500 cm^{-1} , thus maximizing the signal to noise ratio of the IR data obtained from a sample of interest. By combining narrow and wide channel widths in MCFM design, the platform provides fast mixing (460 μs) to induce protein (mis-)folding, and it maximizes the residence time in the observing area, so a wide range of reaction timescales can be captured in a single image. We validated the platform for its ability to induce and observe sub-millisecond processes by studying two systems: (i) the mixing of H_2O and D_2O and (ii) the mixing induced deprotonation of carboxylic acid. First, we observed excellent agreement between simulated and experimental data of the on-chip mixing of H_2O and D_2O , which verifies the distance–reaction time relationships based on simulation. Second, deprotonation of carboxylic acid by on-chip mixing with sodium hydroxide solution validates the ability of the platform to induce rapid pH jump that is needed for some biomolecular reactions. Finally, we studied the methanol-induced partial-unfolding of ubiquitin to show that our platform can be used to study biomolecular events ‘on-pathway’ using FT-IR imaging. We successfully extracted kinetic and structural details of the conformational changes along the channel. Our results are in agreement with prior studies that required more elaborate stopped flow approaches to acquire data for different time points. In summary, the reported method uses an easy-to-fabricate microfluidic mixer platform integrated with hyperspectral FT-IR imaging for rapid acquisition of structural details and kinetic parameters of biomolecular reactions. This approach does not need stopped flow or molecular imaging probes, as required respectively for alternative FT-IR spectroscopy and fluorescence approaches.

 Received 20th February 2019,
Accepted 17th June 2019

DOI: 10.1039/c9lc00182d

rsc.li/loc

Introduction

Fundamental biomolecular events, such as protein folding and enzyme catalysis, are critical for cell and tissue health.¹ Although such biological processes occur on the millisecond

to minute time scales, early intermediates that determine the fate of the overall process often appear within tens of microseconds.² One such event, sub-millisecond protein misfolding, has been shown to lead to a cascade of events that are associated with diseases such as Alzheimer's and Parkinson's that occur due to the presence of plaques composed of aggregated misfolded proteins,^{3,4} *i.e.* β -amyloids. Therefore, studying (mis-)folding mechanisms and identifying the early intermediates are relevant to understanding β -amyloid induced diseases. To study the transition between different protein states, various biophysical techniques have been developed. NMR provides atomic resolution of the reaction process and circular dichroism can reveal secondary structure information of proteins.⁵ Early intermediates within the ‘‘dead time’’ of mixing are difficult to observe, however,

^a Department of Bioengineering, University of Illinois at Urbana–Champaign, 1406 W Green St, Urbana, IL, USA. E-mail: rxb@illinois.edu, kenis@illinois.edu

^b Department of Chemical and Biomolecular Engineering, University of Illinois at Urbana–Champaign, 600 S Mathews Ave, Urbana, IL, USA

^c Beckman Institute for Advanced Science and Technology, University of Illinois at Urbana–Champaign, 405 N Mathews Ave, Urbana, IL, USA

† Electronic supplementary information (ESI) available: Fabrication procedure, micro-CT images of the device, parameters used in the FT-IR imaging set-up, simulation results, and IR spectra from $\text{H}_2\text{O}/\text{D}_2\text{O}$ mixing. See DOI: 10.1039/c9lc00182d

because these methods use stopped flow techniques. To minimize the dead time, continuous flow methods are used, for example for protein folding studies fluorescence microscopy is used.⁶ Such measurement reveals misfolding to be a millisecond time event; however, this approach provides no structural details, and labelling with fluorescence dye may change the folding dynamics.⁷ In contrast, computational models show β -amyloids form at a faster rate. This dissonance may indicate that current methods are insufficient for providing intrinsic structural data for sub-millisecond events.⁸ Hence, experimental techniques need to be developed to study these fast events.

The two main challenges in studying sub-millisecond biomolecular reactions at high structural resolution are (i) achieving sufficient control over the speed of reactant mixing, which determines temporal resolution, and (ii) achieving a sufficient signal-to-noise ratio (SNR) of recorded data, which determines the sensitivity in detecting and identifying reaction intermediates.^{9–11} To meet the first challenge, a technique to mix reactants faster than the reaction kinetics is required.¹² However, widely used mixing methods such as stopped-flow mixers have mixing and dead time delays of a few milliseconds prior to data acquisition.¹³ Continuous-flow mixers are faster, but they consume larger sample volumes that render them unsuitable for most biomolecular reactions.¹⁴ Microfluidic continuous-flow mixers (MCFMs) can be used to mix reactants in microseconds while consuming only nanoliters of sample per minute.

One approach to address the second challenge is IR spectroscopy. However, coupling MCFMs with IR spectroscopy^{15–19} for structural data collection has proven to be challenging. Despite excellent advances with various mixer geometries,^{20,21} practical barriers such as poor compatibility of IR optical windows (often CaF_2) with microfabrication approaches as well as leakage issues encountered at the high flow-rates necessary, continue to persist.^{22–24} Alternative approaches to meet the second challenge that are suitable for rapid data acquisition include fast readout spectroscopic detection methods such as UV-vis absorption and fluorescence. However, they are limited in their ability to provide detailed data on molecular events and often require extrinsic labeling by probes that can potentially alter reaction dynamics.⁷

In this work, we address both challenges to develop and validate a multidisciplinary approach to study biomolecular reactions at sub-millisecond temporal resolution. We report an IR transparent and easy-to-fabricate microfluidic platform that accurately mixes solutions and controls biochemical environments spatially and temporally. The device is used with FT-IR imaging to obtain data on biomolecular events with a good SNR. After experimental and theoretical validation of the platform with two model systems, we showcase the performance of our approach by studying conformational changes of ubiquitin during unfolding.

Results and discussion

Design of polymeric microfluidic continuous flow mixer (MCFM) for studying rapid biomolecular reactions

Various designs of microfluidic platforms, such as laminar flow mixers,^{24,25} herringbone mixers,²⁶ and inertial effects-induced mixers,^{27–29} have been demonstrated to achieve microsecond to millisecond mixing. However, the requirement of (a) small feature sizes (1–10 μm) and (b) high back-pressures (~ 5 MPa) resulting from high flow rates in narrow channels restricts the materials and fabrication processes available to manufacture these devices. Fabrication options are further restricted as IR compatibility for microfluidic platforms mandates the use of materials with low IR absorption.

We decided to use hydrodynamic flow focusing (HFF) design^{30–32} for the application here, as this design enables microsecond mixing (10 μs –10 ms) in the microchannel with relatively large feature sizes (>20 μm) that can be conveniently fabricated with standard microfabrication processes. HFF typically involves focusing of a central analyte stream by two buffer streams on the side, as shown in Fig. 1. This focusing reduces the width of the central stream and consequently the diffusion distances, resulting in faster mixing. In addition, the subsequent laminar flow in the microchannel enables the reaction to evolve without intermixing and it aligns reagents in the center of the channel. Although the small width of the focused stream is beneficial for rapid mixing, this small width may not provide sufficient SNR if the size of the IR detector is larger than or comparable to the stream width. To address this issue, we designed the channel to incorporate a rapid expansion of the stream before introduction in a wide observation zone, 500 μm wide (the length and width of the field of view are about 700 μm) and 10 mm long (the partial channel is shown in Fig. 1). After comparing geometries with 90°, 67.5°, 45°, and 22.5° for the angle to

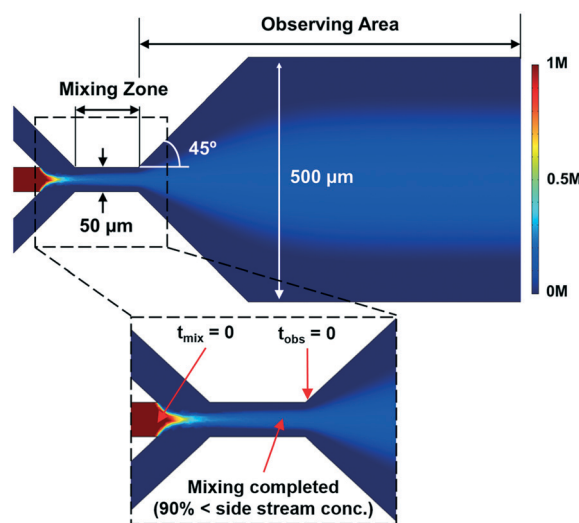


Fig. 1 Schematic illustration of hydrodynamic flow focusing and the designed MCFM. The design includes a 50 μm -wide mixing channel (high-velocity region) for rapid mixing that broadens via a 45° smooth expansion to a 500 μm -wide reduced velocity region (observation area).

expand the channel width into the observation area, the 45° geometry was chosen to minimize the occurrence of turbulent eddies caused by sudden expansion and to allow a wide range of reaction timescales to be captured in a single image (Fig. S4†). This rapid expansion not only increases the width of the analyte stream but also minimizes the required operating backpressures due to the larger width of the expansion and observation channels. We designed the minimum width of the focusing channel to be 50 μm, which can be easily fabricated using standard microfabrication processes and fits with typical fields of view of standard and high-definition FT-IR imaging spectrometers^{33–35} while being narrow enough for emerging FT-IR scanning spectrometers.^{36,37} The width of the observation channel was chosen to be 500 μm, which provided sufficient expansion to ensure a large width of the analyte stream post-mixing as confirmed by finite element analysis (FEA) simulations as well as a sufficient area for spatial signal averaging if required.³⁸ Smaller channel heights will ensure a linear signal from absorption but will also lead to higher back-pressures. To achieve a good SNR and transmission signal from the reagents, we chose the optimal height of the microfluidic channels to be 15 μm, which yields sufficiently low back-pressures that can be withstood by the microfluidic platform.³⁹

MCFM design considerations

Time-to-space mapping. The first demonstration of fast FT-IR imaging measurements in transmission mode that utilized a microfluidics platform to show the applications to detect biomolecular reactions⁴⁰ used rapid scanning “kinetics” mode.⁴¹ A similar approach that utilized laminar and segmented flows also used kinetic scanning mode to study reactions.⁴² In these approaches, it is possible to quantify the time resolution using the reagent delivery flow rate and the pixel size.^{40,42} However, in kinetic scanning mode, the time resolution is limited by the total scanning time for each image, which is ultimately limited by the detector frame rate. Thus, its application is limited to exploring relatively slow reactions. A larger volume of material would be needed in the case of “time-resolved” mode, resulting in inherent lowering of efficiency of recording data.⁴³ Thus, we decided to use an HFF design in combination with the “continuous” scanning mode to acquire information faster while maximizing the SNR. Laminar, steady-state flow conditions enable accurate predictions of the consistent spatial flow and concentration fields of the reagents using computational modelling. At a constant flow rate, the channel attains a pseudo-steady state condition where every point is invariant in the reaction state at that location. Thus, the same location can represent sub-millisecond, millisecond, or second time scale by adjusting the flow rates and ratio from inlets. For example, at a flow rate of 0.1 μL min⁻¹ for the central stream with a flow rate ratio of 1:5 between central and side streams, the 35th pixel represents 47.88 ms and the 100th pixel represents 147.61 ms while for a flow rate of 2.2 μL min⁻¹, the two points represent

0.84 ms and 3.36 ms, respectively. Un-reacted reagents at the junction (the start of the channel) incrementally progress along the temporal reaction coordinate down the channel along the direction of flow (Fig. 1). Hence, the modeling data can be used to estimate the time it takes for reagents to reach any particular spatial coordinate; each spatial coordinate in the device represents a specific point of time (or temporal coordinate) after mixing. The flow and concentration fields of the reactants are precisely determined by solving the steady-state, incompressible Navier–Stokes and convection–diffusion equations with finite element analysis software (COMSOL Multiphysics). FT-IR spectra from pixels at various locations in the image allow us to access multiple time scales in a single experiment, simply by collecting data at a different spatial location. Each location represents a different reaction state that does not change over time, as long as the streams continue to flow. Since the flow velocity obtained from the FEA simulation and the pixel size of the FPA detector are the only parameters required to perform the distance to time conversion, the measurement speed of the instrument does not affect the time resolution.

Optimization of time resolution/image size. To accurately study the kinetics of biomolecular events, reactants need to be mixed faster than the reaction time scale. Thus, one of the primary design considerations for the MCFM is to decouple mixing and kinetics. To ensure this decoupling, the desired time of mixing (t_{mix}) should be at least one order of magnitude lower than the time constant of biological processes (t_{kinetic}). The starting points for mixing ($t_{\text{mix}} = 0$) and observation ($t_{\text{obs}} = 0$) are the points where three inlet streams start to merge and where the narrow channel starts to expand linearly (Fig. 1). Previous microfluidic chips that used hydrodynamic focusing defined t_{mix} as the time it takes to achieve 90% of the side stream concentration in the focused stream.³⁰ Here we exploit the same concept. From mass conservation and diffusion over distance equations reported for hydrodynamic focusing,⁴⁴ we derived an equation that can be used to calculate the mixing time for the MCFM platform:

$$\tau_{\text{mix}} \sim \frac{w_f^2}{4D} \approx \frac{1}{4D} \frac{v_o^2}{v_f^2} \frac{w_o^2}{(1+2\text{FRR})^2} \quad (1)$$

where

τ_{mix} : mixing time

D : diffusion coefficient

w_f : width of the focused stream

w_o : width of the mixing channel

v_f : average velocity of the focused stream in the mixing channel

v_o : average velocity at the end of the mixing channel

FRR: flow rate ratio between side and center inlets

From eqn (1), it is evident that the mixing time is inversely proportional to the diffusion coefficient and varies inversely with the square of the flow rate ratio and of the concentration of side streams.

Another design consideration for the MCFM platform is that the temporal scale should correspond to the size of the hyperspectral image so that the kinetics can be observed in a single image. Each pixel of the FPA detector images an area of $5.5 \times 5.5 \mu\text{m}^2$ when using a $15\times$ objective. Thus, the size of the entire hyperspectral image (the area of the channel that is being imaged) is $704 \times 704 \mu\text{m}^2$ (128×128 pixels). However, due to the diffraction, the actual area imaged by one pixel can be different from the pixel size. Based on the Rayleigh criterion and 0.62 N.A. used in the set-up, the range of the spatial resolution is approximately equal to the wavelength, and thus the area imaged by one pixel can vary depending on the selected vibrational mode. These two criteria (or design considerations) then provide the timespan of the device and suggest that the mixing time should be at least one order of magnitude lower than this time span. While a larger image can be acquired by rastering the sample,⁴⁵ moving the stage of the microscope may introduce errors and may cause periods of unsteady flow due to device movement. Hence, observing the overall event without moving the focal plane array (FPA) view is another important aspect to consider when designing the device.

With the FEA simulation and eqn (1), in our case, the theoretically fastest mixing time that fulfils both criteria is about $460 \mu\text{s}$, corresponding to a residence time for a single FPA image ($704 \times 704 \mu\text{m}$) of 4.8 ms, a significantly better mixing time and residence time compared to what has been reported previously for other microfluidic platforms.^{33,42,46} The change in residence time for the observation area as a function of the flow rates used can be found in Fig. S5.† Among available microfluidic platforms that have been used with IR imaging, the fastest reported mixing time is $280 \mu\text{s}$,⁴⁶ which does not fulfil the consideration that the time at the end of the image needs to be larger than t_{mix} . Because of the fast speed of the central focused stream (needed to achieve such rapid t_{mix}), the time resolution of the FPA image is limited and does not allow data collection of the full reaction in a single image. Even though the fastest mixing time in our platform design is slightly slower than the aforementioned $280 \mu\text{s}$, the spectral data from our platform will provide better signal quality without loss of information regarding early intermediates.

Polymeric MCFM: IR transparency and robustness

We collect IR data in transmission mode because of its ease of implementation, limited spectral distortion for homogeneous phases, and good spatial resolution.^{46,47} However, this mode requires the use of IR transparent materials and a shallow channel height ($\sim 10 \mu\text{m}$) for aqueous solutions.^{39,48} Previously reported IR compatible microfluidic platforms use calcium fluoride (CaF_2) windows, because of their IR transparency in the biologically relevant region, but CaF_2 is expensive, not very amenable to rapid prototyping, and is hard to bond with itself or other substrates.^{24,49} Typical microfluidic platforms based on CaF_2 windows have channel heights greater than $50 \mu\text{m}$, whereas a shorter path length is needed

for best data collection results.⁴⁰ To overcome the aforementioned issues, we created a MCFM out of two $100 \mu\text{m}$ cyclic-olefin copolymer (COC) films that sandwich a thin poly(dimethyl siloxane) (PDMS) fluid layer that is patterned to contain the desired microfluidic channel design. Though PDMS absorbs IR in the biologically relevant region ($1500\text{--}2500 \text{cm}^{-1}$), the use of an only $15 \mu\text{m}$ thick layer of PDMS minimizes IR absorption, while allowing for a channel height that provides a sufficient SNR. The stiff COC film provides mechanical robustness (less fragile than CaF_2) and allows for easy prototyping and fabrication. The ability to mount in and outlets on/through the COC sheets enables the use of microfluidic channels with heights less than $20 \mu\text{m}$ between the COC sheets, a thickness that is optimal for transmission IR data collection. We confirmed that the assembly of COC and PDMS layers provides a sufficiently IR transparent window over $1500\text{--}2500 \text{cm}^{-1}$ (Fig. 2) and beyond 3100cm^{-1} ; it will allow for IR data of organic species and the secondary structure of different proteins (*e.g.*, the amide I region) of sufficient SNR to be recorded. To ensure strong bonding between the PDMS and COC layers, we used a chemical bonding approach (APTMS-GPTMS) that previously has been demonstrated to sustain high pressures ($>0.5 \text{MPa}$) without leakage for microfluidic PDMS-COC platforms.^{50,51} We confirmed that the fabricated MCFM can withstand flow rates as high as 22m s^{-1} without leakage by flowing dyed aqueous solutions. A detailed description of the fabrication of the MCFM platform is provided in the experimental section (*vide infra*). The detection range that can be assessed with the MCFM platform is limited. Specifically, due to lack of transparency, data cannot be collected with the FT-IR imaging approach used in the regions of $600\text{--}1500$ and $2800\text{--}3100 \text{cm}^{-1}$. However, the MCFM

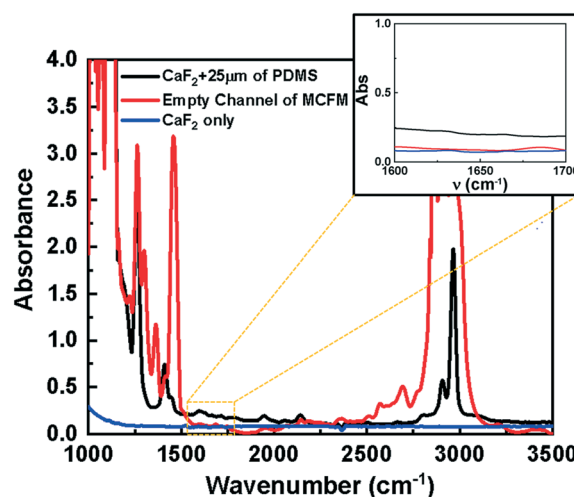


Fig. 2 IR spectra of the MCFM platform, CaF_2 only, and $\text{CaF}_2 + 25 \mu\text{m}$ PDMS. The spectra of CaF_2 and CaF_2 with a thin PDMS layer are provided here to allow for direct comparison of the relative transparency of the MCFM platform to materials used in prior work. The chip is largely transparent in the region of $1500\text{--}2500 \text{cm}^{-1}$ and beyond 3100cm^{-1} , especially between 1600 and 1700cm^{-1} (a major detection region for the secondary structure of proteins). The spectra are taken in transmission mode with an air background.

platform has a similar detection range compared to previously reported IR compatible microfluidic platforms that utilize either CaF_2 or Si wafers, because all of them require the use of PDMS to create channels between wafers and to provide the bonding between layers.^{52,53} In addition to similar IR transparency, the MCFM platform reported here offers mechanical robustness and easier prototyping of channel designs that allow for rapid mixing as well as simultaneous observation of a wide range of reaction times than the aforementioned previously reported platforms.

Validation system 1: mixing of H_2O and D_2O

An appropriate method to model diffusional mixing of species in the MCFM is needed to be able to correlate spatially resolved FT-IR imaging data to temporally resolved information mapping the studied chemical process. As a first test to validate the use of the MCFM platform in combination with IR imaging, we studied the mixing of H_2O and D_2O both experimentally and *via* simulation, the latter using finite element analysis. The IR absorption arising from both the $-\text{OH}$ and $-\text{OD}$ vibrational modes changes in tandem upon mixing, as has been reported previously.³³ Similarly, we anticipate a change (drop) in IR absorbance at 1645 cm^{-1} arising from the OH bending vibrational mode, from both a change in concentration (dilution with D_2O) and due to isotopic substitution (H and D).^{33,46} As H_2O and D_2O mix, HDO is produced and the spectrum of the HDO bending mode appears at 1451 cm^{-1} .³³ Though absorption at 1451 cm^{-1} is another indicator to show the mixing of H_2O and D_2O , we do not discuss the change in the HDO spectrum here, as this has been reported previously.³³ Furthermore, due to the high absorption of the MCFM platform at 1451 cm^{-1} , this mode would not be examinable with this platform.

Inside the MCFM, streams of pure H_2O and pure D_2O were injected through the central and side channels, respectively, at flow rates of 0.4 and $2.0\text{ }\mu\text{L min}^{-1}$. Fig. 3a shows the relative absorbance of the two vibrational modes, OH bending and OD stretching. We picked the OD stretching vibration and not the OD vibration due to overlap of the latter with vibrations from the MCFM materials. The observed change in absorbance nicely visualizes hydrodynamic focusing and mixing inside the channel (Fig. 3a). The combined effect of diffusion-induced hydrodynamic mixing can be monitored by examining the change in absorbance along the hydrodynamic jet. The IR absorbance of OH bending, quantified by the area-under-the-curve (AUC) from each pixel along the focused stream, decreases exponentially as can be seen in Fig. 3b. Because of the difficulty of experimentally measuring the exact flow velocity at different locations, we performed a FEA simulation of the same experiment to aid the distance to time conversion. Naturally, the experimental data and results from the simulation should overlap. The simulation shows that upon the onset of mixing of H_2O with D_2O , the concentration of H_2O decays exponentially along the channel (Fig. 3b, solid blue line). As expected, the experimental data match the simulated water concentration. Note that the time-

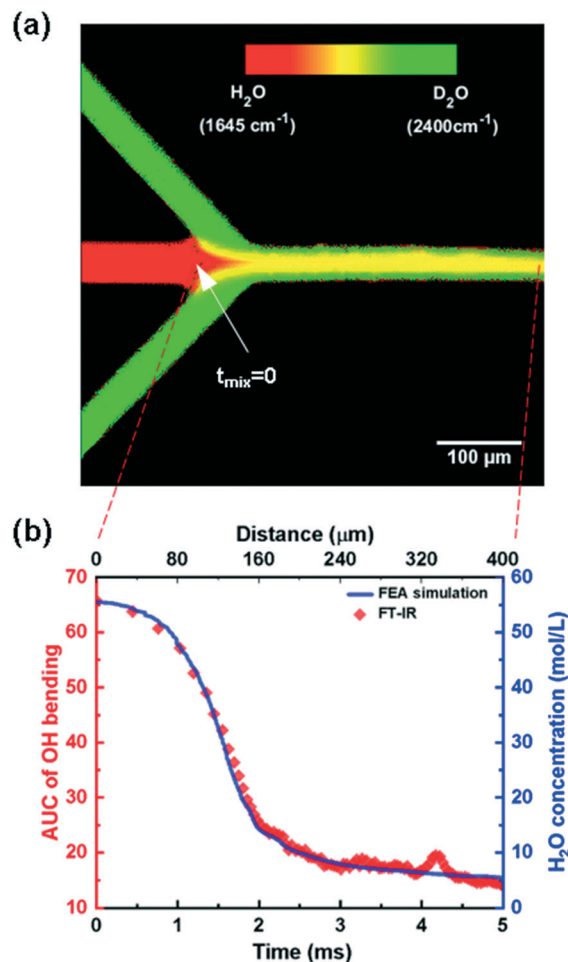


Fig. 3 Experimental observations and simulation of H_2O and D_2O mixing inside the MCFM. (a) Hyperspectral image of the mixing zone, showing the ratio of absorbance at 1645 cm^{-1} and at 2400 cm^{-1} corresponding to the OH bending vibrational mode in H_2O and the OD stretching vibrational mode in D_2O . (b) Comparison of experimental data (red diamonds, AUC of IR spectra from OH bending; average of three data sets) and simulation (blue line) of diffusional mixing of $\text{H}_2\text{O}/\text{D}_2\text{O}$. The error in the experimental data points (red diamonds) is smaller ($<1.7\%$) than the size of the diamonds.

scale used in Fig. 3b was derived from the velocity profile obtained in the FEA simulation.

In summary, the RGB image (Fig. 3a) and the comparison of the FT-IR results and the simulation (Fig. 3b), indicate that the MCFM platform successfully mixes streams *via* hydrodynamic focusing, and that with the use of the simulation results, the distance along the axis of flow can be converted into a reaction timescale. Furthermore, it is evident that in the middle of the channel a fully mixed situation is reached after about 3 ms under these operation conditions.

Validation system 2: acetic acid and pH jump

As a second test to validate the use of the MCFM platform to monitor chemical events, we studied the deprotonation of acetic acid upon mixing with an aqueous NaOH stream.

While the previous example allowed us to control the concentration in the two streams and demonstrated that FEA simulations and experimental results agree well for a system in which the properties of the materials are close, this second system seeks to highlight the ability of the platform to control environmental conditions such as pH to induce a biomolecular reaction.⁵⁴

Approaches to initiate biomolecular reactions include changing the temperature, adding a denaturant, and changing the pH surrounding the molecules. Inducing and maintaining a sudden temperature change in a MCFM would be challenging from a temperature control point of view due to the small amount of sample available. Denaturants such as guanidinium chloride (GuHCl) and urea have high absorption in the amide I region (1600–1700 cm^{-1}), which would complicate secondary structure determinations of proteins.⁵⁵ Biomolecular reactions are also sensitive to the pH value of their solvents; under acidic and basic conditions, protonation or deprotonation of amino acid residues occurs and changes their participation in hydrogen bonding. Hence, a pH jump strategy can be used to induce reactions such as protein folding/unfolding, protonation/deprotonation, and enzymatic reactions.

To validate the application of the MCFM platform to study biomolecular reactions, we designed an experiment in which the pH is changed in the stream by hydrodynamic flow focusing induced mixing between 1 M aqueous acetic acid solution ($\text{p}K_{\text{a}}$ 4.76) as the central stream and 0.15 M aqueous sodium hydroxide solutions as the side streams. A flow rate ratio of 1:5 between central and side streams and a flow rate of 3.0 $\mu\text{L min}^{-1}$ for acetic acid solution were used. This experiment is expected to increase the pH from 2.5 to neutral at the center of the focused stream after complete mixing. When a carboxylic acid group reacts with a hydroxide ion, it deprotonates and becomes a carboxylate. Since a carboxylic acid (1718 cm^{-1}) and a carboxylate (1556 cm^{-1}) have distinct vibrational modes corresponding to the carbonyl stretch ($\nu_{\text{C=O}}$) and the asymmetric mode of the carboxylate anion, respectively, the absorbance of these modes can quantify the extent of change in the pH along the center of the channel in the MCFM for inducing biomolecular reactions.

Fig. 4 shows the results of the pH jump experiment. The peak IR intensities for carboxylic acid (1718 cm^{-1}) and for carboxylate (1556 cm^{-1}) are used to generate the respective color maps that visualize the concentration distribution of the carboxylic acid (Fig. 4a) and the carboxylate (Fig. 4b). To enhance the color gradient in these color maps, the second derivative of the spectra was taken, and signs were reversed, as this maximizes the IR intensity difference between two peaks and overlapping OH bending spectra and removes any baseline effects. Similar to the H_2O and D_2O mixing experiment described above, the point of complete mixing is reached $\sim 250 \mu\text{m}$ from where the three inlets merge when a 1:5 flow ratio between the central and the side channels is used. Fig. 4c, which shows IR spectra of pixels along the center line of the MCFM platform, nicely visualizes the deproton-

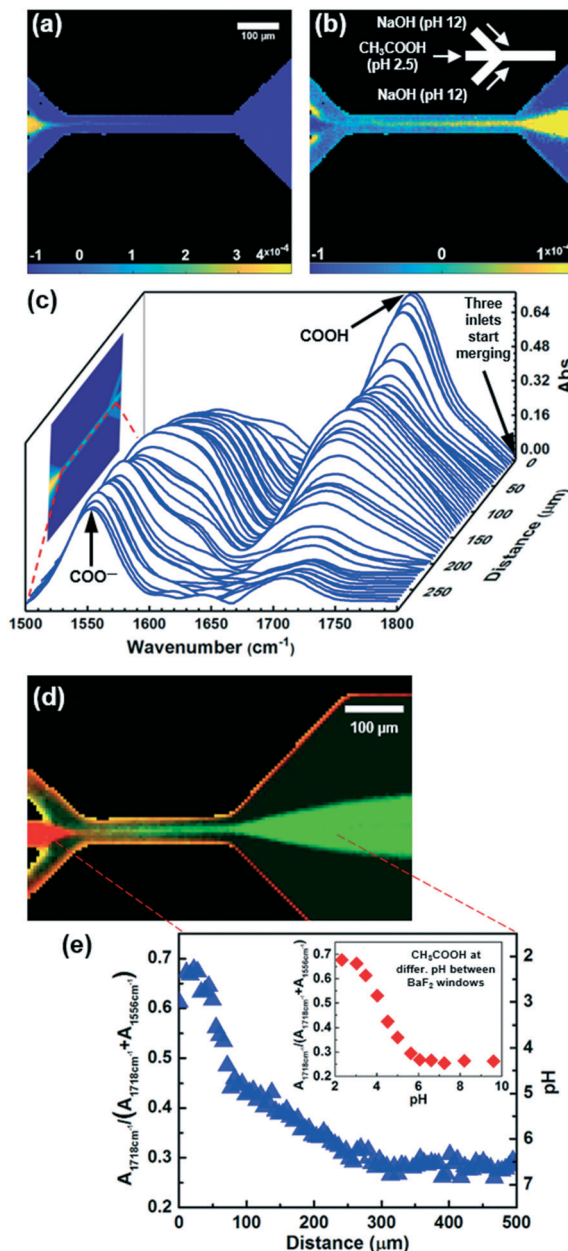


Fig. 4 Validation of the feasibility of MCFM platforms for pH jump experiments that can be used to induce biomolecular reactions. (a) and (b): Color maps of the second derivative of carboxylic acid (1718 cm^{-1}) and carboxylate (1556 cm^{-1}) peak IR intensities, respectively, in the MCFM platform. (c) FT-IR imaging data (after water subtraction and baseline correction) that visualize acetic acid deprotonation (disappearance of the carboxylic acid peak) down the center of the channel in a MCFM platform. (d) Color map of pH changes in the acetic acid deprotonation experiment. (e) Graph of the ratio of the carboxylic acid and carboxylate peak IR intensities along the center line. Inset: identical ratio of peak intensities from acetic acid solutions at different pH values; data used to determine the local pH in the MCFM data.

ation experiment: the appearance of the carboxylate peak and the disappearance of the carboxylic acid peak is evident. This waterfall plot (x-axis: wavenumber, y-axis: absorbance, and z-axis: distance) shows that the 1718 cm^{-1} peak intensity decreases and that the dominating peak shifts to 1556 cm^{-1}

after 200 μm from the point where the three streams merge. The pH of the focused stream has changed from acid to neutral at that point.

To visualize changes in the pH within the focused stream, the ratio between the carboxylate and carboxylic acid peak IR intensities is calculated and converted into a color map (Fig. 4d). Next, we plotted the pixel values of this ratio of peak IR intensity data along the center line. In order to be able to correlate these data with local pH we first collected the IR spectra of individual acetic acid solutions at different pH values between BaF_2 windows with a standard FT-IR spectrometer. The ratio between the carboxylate and carboxylic acid peak IR intensities of these acetic acid solutions is calculated (the inset plot with red diamonds in Fig. 4e). By correlating the peak IR intensity ratios of the MCFM experiment and of the stock solutions (BaF_2 windows), we can determine the local pH at each point along the center line of the MCFM platform (the right axis of the graph in Fig. 4e). The color gradient (from red to green, Fig. 4d) rapidly changes as soon as the central stream is focused by the side streams. A uniform zone of neutral pH (complete mixing) is reached at 250 μm in the focused stream, as is evident in both the color map (Fig. 4d) and the graph that plots the ratio of the peak IR intensities along the center line (Fig. 4e). Based on the flow rate used and the point where complete mixing occurred in this pH jump experiment, one can calculate that complete mixing is achieved after 529 μs .

In summary, the results of the pH jump experiment shown in Fig. 4 demonstrate the ability of the MCFM platform to rapidly change the pH of a focused stream. This approach can be applied to initiate and study biomolecular reactions that are induced by a pH change of the surrounding solvent.

Application of MCFM and FT-IR imaging: ubiquitin unfolding

After completing the validation experiments, we sought to demonstrate the application of the MCFM platform to the study of biomolecular reactions. Specifically, we decided to study the unfolding of the well-studied protein ubiquitin. Ubiquitin is a small 76-residue protein molecule with a highly stable native structure that changes its conformation when exposed to organic solvents under acidic conditions.²³ Ubiquitin, when dissolved in an aqueous methanol solution at low pH is partially unfolded (A-state) if the methanol concentration exceeds 30%.⁵⁶ Hence, we prepared 7 mg mL^{-1} ubiquitin in 20% methanol- d_4 and 80% D_2O solution (pD adjusted to 2 with DCl). This solution is delivered through the central inlet of the MCFM. Two side stream solutions of 70% methanol- d_4 and 30% D_2O (pD adjusted to 2 with DCl) focus the central stream. The goal is to change the concentration of methanol to above 30% in the central stream to induce the partial unfolding of ubiquitin, as is shown schematically in Fig. 5a, using FEA simulation. The flow rates for the central and side streams are all set to 0.08 $\mu\text{L min}^{-1}$.

To determine the vibrational signatures of the native and A-state of ubiquitin, respectively, we first collected IR data from the central channel from a point before it was exposed to the side streams and from a point well after complete mixing was reached (Fig. 5b: 'before mixing' and 'after mixing' data). For reference, we also collected IR data of identical ubiquitin solutions in the native and A-state in a cell with BaF_2 windows (Fig. 5c). These data are in agreement with spectra reported in the literature.²³ Four major components are present within the amide I region of the ubiquitin spectra: peaks with wavenumbers of ~ 1630 , 1642, 1650, and 1665 cm^{-1} that arise from the CONH vibrational mode of a β -sheet, a random coil, an α -helix, and a β -turn, respectively. Since deuterated solutions are used to prevent the OH bending mode from interfering with the recording of the amide I region, the isotope exchange between H and D is inevitable and deuterium can be also considered as a biasing agent in kinetic studies. The peaks in the amide I region arise mainly from C=O stretching, with minor contributions from out of phase C-N stretching and in-plane N-H bending.⁵⁷ Hence, the effect of the isotope exchange on the kinetic data in the amide I region is small and the bias from using deuterated solutions should be less than, for example, the influence induced by labels used in fluorescence measurements. N-D bending and stretching vibrations that arise due to isotopic exchange cannot be observed due to the broad D_2O absorbance and materials used in the MCFM platform. To obtain detailed information on the secondary structure of ubiquitin upon mixing with the side streams, IR data are collected along the center of the channel. Data for two intermediate states are shown in Fig. 5b. Data for two intermediate states are shown in Fig. 5b. Voigt curve fitting⁵⁸ is conducted for all spectra obtained along the center line. Data for two of the intermediate states as well as from a point before mixing and a point after complete mixing are shown in Fig. 5b. These fits already show that the β -sheet fraction decreases upon dilution with methanol, and that the α -helix and β -turn fractions increase, all indicative of the partial unfolding of ubiquitin. Increase in the β -turn content is likely due to the effect of methanol, which lowers the folding free energy level of β -turn and promotes its formation.⁵⁹

To obtain kinetic information on the partial unfolding process of ubiquitin, we calculate the area-under-the-curve (AUC) for each β -sheet (1629 cm^{-1}) and α -helix (1650 cm^{-1}) from the deconvoluted spectra at every pixel along the center line starting from the start of the diverging, wide section of the channel, where we know (from FEA) that the solution is completely mixed at the center. We then plot these AUC data as a function of time (Fig. 5d). This timescale was calculated using the time-to-space mapping procedure outlined in the section on MCFM design considerations, using the FEA simulation data shown in Fig. 5a. The AUC data in Fig. 5d clearly show that the fraction of the β -sheet and α -helix respectively decreases and increases over time. Both are indicative of the structural change of ubiquitin from the native to the A-state.²³ Single exponential fitting yielded time constants for

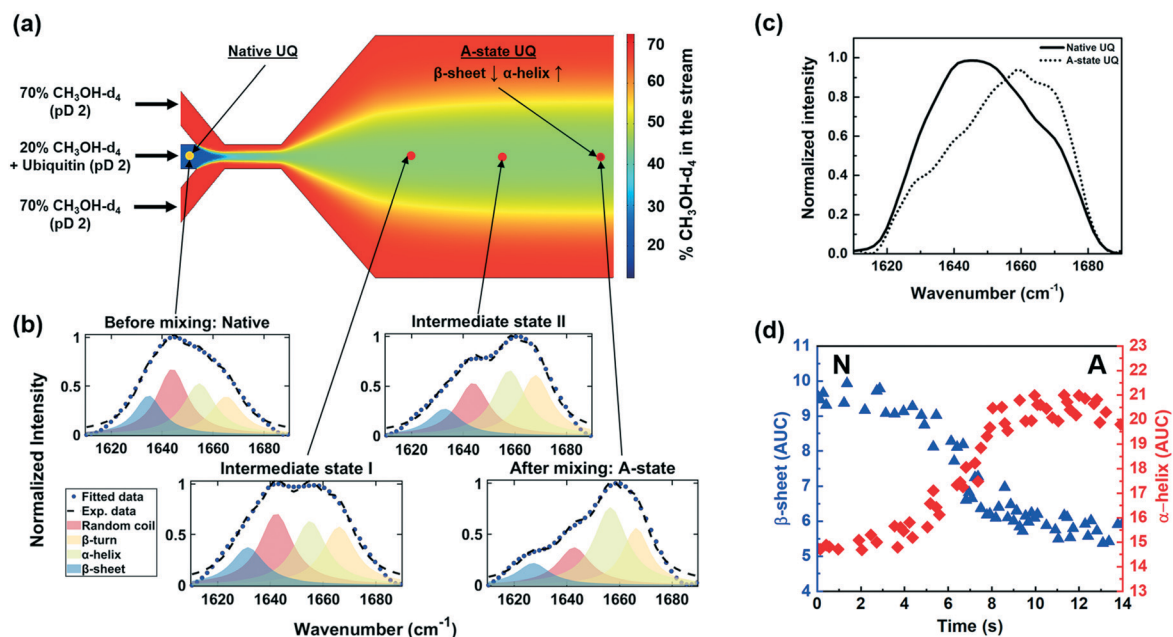


Fig. 5 Conformational change of ubiquitin from native to A-state induced by methanol under acidic conditions in the MCFM platform. (a) Visualization of the ubiquitin conformational change experiment (COMSOL simulation). Ubiquitin is dissolved in 20% methanol-d₄ (pD 2) in the central stream and mixed with side streams of 70% methanol-d₄ (pD 2) to increase the percentage of methanol of the focused stream up to 50%, which induces a conformational change. (b) Curve fitted IR spectra at different points along the center channel: before mixing, two intermediate states, and a point well after complete mixing. All spectra were baseline corrected, normalized, and de-convoluted to analyse any changes in the secondary structure of ubiquitin. (c) Reference spectra of ubiquitin for the native (solid) and the A-state (dot) obtained from solutions with BaF₂ windows. All data were background corrected and normalized. (d) Graphs that show kinetic IR data of the area-under-the-curve for the deconvoluted β-sheet and for α-helix peaks representing, respectively, the disappearance of the β-sheet and the appearance of the α-helix, both key identifying features of the native (N) and A-state (A) of ubiquitin.

the kinetic data of β-sheet disappearance and α-helix appearance of 0.28 s⁻¹ and 0.26 s⁻¹, respectively. The time constant for the α-helix closely matches the kinetic data obtained from NMR experiments that followed Tyr-59 (0.25 s⁻¹), a residue

that is located at the end of the α-helix, as an indicator of ubiquitin conformational change.⁶⁰

The results of the partial unfolding of ubiquitin demonstrate the ability of the MCFM platform to obtain both

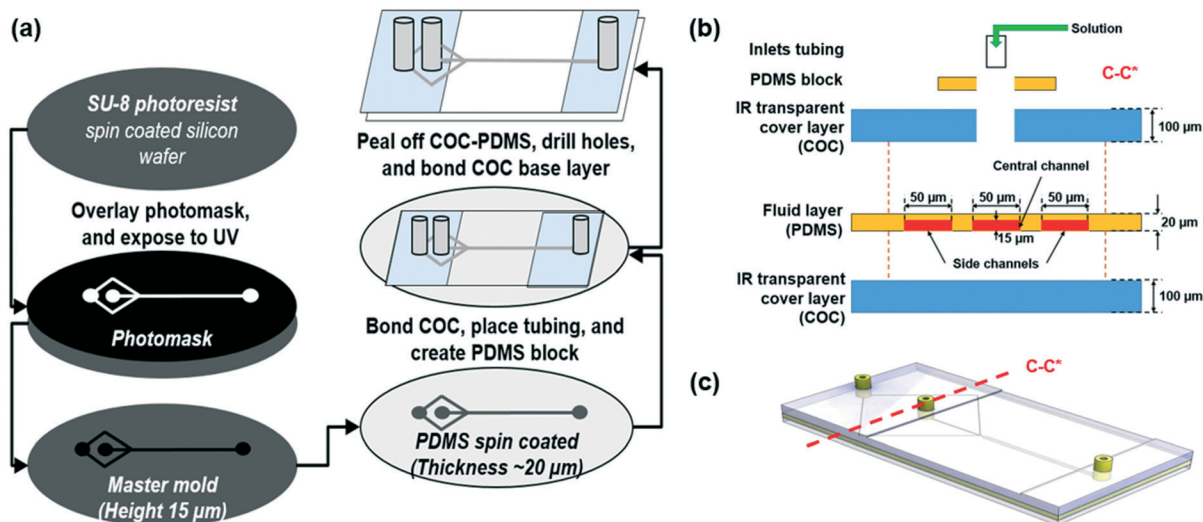


Fig. 6 (a) Fabrication scheme for the MCFM platform. A standard photolithography technique was used to create the master mold with a 15 μm channel height using silicon wafer and a negative photoresist. The PDMS (15 : 1) layer (20 μm) was spin coated on the master mold and bonded with COC using covalent amine-epoxy chemistry. Tubing for inlets and outlet was placed and bonded with extra PDMS around them. The COC-PDMS layer was peeled off and bonded with the bottom COC layer, again using covalent amine-epoxy chemistry. (b) Cross section (red dashed line on Fig. 5c) showing different layers of the device. (c) 3D view of the assembled device.

structural changes and kinetic information on biomolecular events, although this only was a relative slow process.

Experimental

Fabrication procedure of the MCFM

We used standard photolithography⁶¹ to create a master mold with a channel height of 10–20 μm on silicon wafers using an SU-8 (25) photoresist (MicroChem Corporation). A thin layer (~ 15 – $25 \mu\text{m}$) of PDMS (General Electric Company) was spun on the SU-8 master mold, cured on a hot plate at 80 $^{\circ}\text{C}$, and plasma cleaned (Fig. 6a). A 100 μm thick COC sheet (TOPAS Advanced Polymers Inc) was also plasma cleaned and bonded to the PDMS layer using covalent amine-epoxy chemistry,⁴⁶ resulting in a PDMS–COC bond that can sustain high pressures ($>5 \text{ MPa}$) without leakage. The composite COC–PDMS layer was peeled off, and PEEK tubing was bonded on the COC side using PDMS to hold the tubing in place. Next, the inlet and outlet holes were punched. Finally, the assembly was bonded to a flat COC sheet, again using the aforementioned covalent amine-epoxy chemistry, yielding the composite COC–PDMS–COC device; a cross section is shown in Fig. 6b and a perspective view is shown in Fig. 6c. Details for the fabrication procedure can be found in the ESI.† Being able to reproduce the MCFM platform, including exact layer thicknesses, is important because the optical path length depends on the thickness of the PDMS layer. To demonstrate the uniformity of the thickness of the PDMS layer in the MCFM, micro-CT images of inlets, as well as the narrow mixing channel, and the wide observation channel are presented in Fig. S2.†

MCFM operation

Reactant solutions were loaded into syringes (BD 1 mL) and PEEK tubing (Fisher Scientific Company LLC) was used to connect the syringes to their respective inlet ports on the MCFM platform. Syringe pumps (Micro-Liter OEM Syringe Pump Modules, Harvard Apparatus), controlled independently *via* custom software, delivered a constant flow rate needed to establish and maintain a hydrodynamic flow focused stream (Fig. 7).

H₂O and D₂O mixing experiment. Pure DI water and D₂O (MilliporeSigma) were delivered through the center and side channels, respectively, at flow rates of 0.4 and 2.0 $\mu\text{L min}^{-1}$ to achieve mixing *via* hydrodynamic focusing.

Acetic acid and pH jump experiment. Glacial acetic acid (99.8%; MilliporeSigma) was mixed with DI water to adjust the concentration to 1 M (pH 2.5). To achieve a neutral pH in the focused stream after complete mixing, side stream solutions of 0.15 M sodium hydroxide (ACS reagent, $\geq 97.0\%$, pellets; MilliporeSigma) were used. The acetic acid and NaOH solutions were delivered through the central and side channels, respectively, with a 3.0 $\mu\text{L min}^{-1}$ flow rate for the central stream and a central:side flow rate ratio of 1:5 to validate the rapid pH change from 2 to 7 in the focused stream.

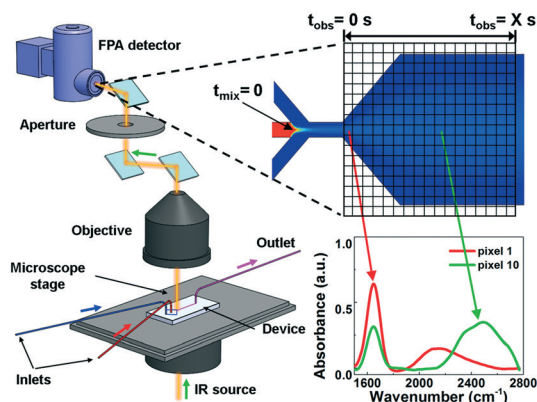


Fig. 7 Overall set-up and data acquisition of hyperspectral FT-IR imaging in transmission mode combined with the microfluidic device. The grid represents 128×128 pixels of FPA and two different spatial locations (pixels 1 and 10) show distinct infrared spectra.

Ubiquitin partially-unfolding experiment. 7 mg mL^{-1} ubiquitin from bovine erythrocytes (MilliporeSigma) was dissolved in a mixture of 20% (v/v) methanol-*d*₄ (MilliporeSigma) and 80% D₂O, and the pD was adjusted to 2 with diluted DCl (20% w/w in D₂O, 99.5%; Thermo Fisher Scientific Chemicals). To induce the conformational change of ubiquitin, a solution of 30% D₂O and 70% methanol-*d*₄ was prepared for the side streams and the pD was also corrected to 2. Flow rates of 0.08 $\mu\text{L min}^{-1}$ were used for both center and side streams to result in a focused stream of 50% methanol-*d*₄ (pD 2) after complete mixing. Only deuterated solutions were used because high absorption of the OH bending vibration in H₂O conceals the detection region for the secondary structures of different proteins.

Data collection and data analysis

When an FT-IR microscope equipped with a focal plane array (FPA) detector is combined with flow cells that allow data collection in attenuated total reflection (ATR)³³ or transmission¹⁵ mode, it can track chemical reactions at different locations by generating spectral images. Here, to enable data collection from multiple locations along the channel simultaneously, FT-IR imaging was performed using an Agilent Cary 620 FT-IR microscope equipped with a 128×128 pixel focal plane array (FPA) detector (Fig. 7).^{62–65} The image was collected with a 4 cm^{-1} resolution, 64 scans, and standard magnification under a 15 \times objective in transmission and continuous scanning modes. To obtain t_{mix} and t_{kinetic} , the central lines in both the narrow mixing channel and the wide observation area are selected. For t_{mix} , the FPA view is adjusted to capture both points where, respectively, the three streams start to merge and where the narrow channel ends. For t_{kinetic} , the left end of the FPA view is adjusted to be placed from where the channel starts to expand linearly (Fig. 1). Distance to time conversion is performed based on the FPA pixel size and flow velocity obtained from the FEA simulation. Hence, compared to a kinetic scanning mode set-up, the time

resolution in our platform is not limited by the detector frame rate (which determines the total time for spectral scanning and thus limits the time resolution).^{40,42} Data analysis was performed using FEA simulation data, and the use of custom software modules for ENVI IDL 7.1 and MATLAB. An automated workflow was developed for performing baseline correction, spectral deconvolution, and extracting the reaction kinetics.

Finite element analysis simulations for optimization of operating flow rates and determination of spatial and temporal coordinates of the reagents

To simulate the hydrodynamic focusing and optimize the time resolution for the mixing process, finite element software (COMSOL Multiphysics Version 4.3b; COMSOL, Inc) was used. The steady-state, incompressible Navier–Stokes and convection–diffusion equations were applied to a ‘reacting flow, diluted species’ model and were solved to simulate the concentration and velocity changes in the focused stream depending on the flow ratio and rate and initial concentrations at the central and side inlets. For the range of operating flow rates here, the flow in the microfluidic devices will always be laminar and hence we used the laminar flow option. We performed the simulations in 2D, an assumption that will result in an error in a variation of less than 10% in the mixing time, compared to the time values obtained assuming a 3D flow.⁶⁶ Details about the parameters and results of the simulation can be found in the ESI.†

Conclusions

We reported here the development and testing of a polymeric microfluidic continuous-flow mixer (MCFM) that is compatible with FT-IR imaging and can record biomolecular reactions over a wide range of timescales. This platform uses cyclic olefin copolymer (COC) film as an IR transparent window that can be fabricated in less than a day using fairly readily available fabrication tools. The channel design exploits hydrodynamic flow focusing to achieve fast mixing and to align reagents to the center of the channel. By widening the channel after sufficient mixing in the initial, narrow region of the channel has been achieved, the residence time of reagents in the observing area is increased so that biomolecular reactions that occur over multiple timescales can be observed in a single FT-IR image.

To validate the platform, a H₂O and D₂O mixing experiment was conducted. We also simulated this experiment using FEA. The experimentally observed change in IR absorption of the OH bending mode is in good agreement with the simulation results. The agreement also confirms that simulated data can be used to convert the distance to time in the analysis of biomolecular reactions. The feasibility of the MCFM platform to initiate and study biomolecular reactions induced by a change in pH was validated with an acetic acid pH jump experiment.

Finally, we applied the MCFM platform to successfully monitor the partial unfolding of ubiquitin, specifically the associated conformational change from the native state to the A-state induced upon dilution with MeOH. The observed changes in IR intensity and wavenumber associated with the secondary structure of the protein are in close agreement with previous reports.

The aforementioned experiment demonstrates that the MCFM platform can be used to explore relative slow (of the order 10⁻¹ s⁻¹) biomolecular reactions. As mentioned in the section on platform design, the theoretical fastest mixing time that still satisfies our design constraints of (i) decoupling mixing and kinetic times and (ii) achieving sufficient residence time in a single FT-IR image is about 4 × 10⁻⁴ s. This implies that fast biomolecular reactions, of the order 10⁻³ s⁻¹, can be studied with this platform in a single FT-IR image. Pushing the limits, the MCFM platform should be able to provide insight into biomolecular processes that happen on the order 10⁻⁴ s⁻¹. From the pH jump experiments, we know that the pH of the focused stream can be changed in about 5 × 10⁻⁴ s (529 μs) by the end of the narrow mixing channel, which is close to the fastest mixing time (460 μs) that the platform can theoretically achieve. The color maps in the pH jump experiment, illustrating the deprotonation of carboxylic acid and the pH change in the central stream, demonstrate that the platform can be controlled such that conditions that are appropriate for fast biomolecular processes can be achieved. In the ubiquitin unfolding study, the platform proved its ability to retrieve biological information from IR spectra by showing a conformational change of the protein, including changes in its secondary structures. Hence, from two different experiments, pH jump (fast mixing time) and ubiquitin unfolding (spectra showing a conformational change), the platform demonstrates its potential to explore fast biomolecular reactions.

The MCFM platform reported here should be generally suitable to the study of fast biomolecular reactions. The rate of mixing of the species that induces the biomolecular reaction of interest is determined by the concentration of this species in the side streams, its diffusion constant, and the width of the focused stream, set by the flow rate ratio between the center stream and the side streams (eqn (1) in the section on MCFM design considerations). For example, studying the denaturation of a wide variety of proteins under the influence of small molecules would be of interest.^{67,68} In addition to the application of the MCFM to study conformational changes of the protein, application of the reported microfluidic platform utilizing FT-IR imaging can be extended, for example, to studying the morphological effect of lipid-based drug delivery systems on protein, as well as other processes such as protein crystallization.^{69,70}

Conflicts of interest

There are no conflicts to declare.

Acknowledgements

The authors would like to thank Dr. Prabuddha Mukherjee and Dr. Caitlin Davis for advice regarding platform validation, and Dr. Ayanjeet Ghosh for advice on data analysis.

References

- M. Gruebele, K. Dave and S. Sukenik, *Annu. Rev. Biophys.*, 2016, **45**, 233–251.
- K. Henzler-Wildman and D. Kern, *Nature*, 2007, **450**, 964–972.
- G. Irvine and O. El-Agnaf, *Mol. Med.*, 2008, **14**, 1.
- S. Ferreira, M. Vieira and F. De Felice, *IUBMB Life*, 2007, **59**, 332–345.
- L. Greene, *Rapid mixing methods for exploring the kinetics of protein folding*, Elsevier, San Diego, Calif., 2004.
- L. Greene, *Investigating protein folding, misfolding and nonnative states: experimental and theoretical methods*, Elsevier, San Diego, Calif., 2004.
- H. Ma and M. Gruebele, *Proc. Natl. Acad. Sci. U. S. A.*, 2005, **102**, 2283–2287.
- G. Bowman, V. Voelz and V. Pande, *J. Am. Chem. Soc.*, 2011, **133**, 664–667.
- G. Voth and R. Hochstrasser, *J. Phys. Chem.*, 1996, **100**, 13034–13049.
- N. Moonen and F. Diederich, *Org. Biomol. Chem.*, 2004, **2**, 2263–2266.
- A. Johansson, M. Hogbom, J. Carlsson, R. Gennis and P. Brzezinski, *Proc. Natl. Acad. Sci. U. S. A.*, 2013, **110**, 8912–8917.
- P. Atkins and J. De Paula, *Atkins' Physical chemistry*, Oxford University Press, 10th edn, 2014.
- B. Hill, J. Hill and R. Gennis, *Biochemistry*, 1994, **33**, 15110–15115.
- M. Shastri, S. Luck and H. Roder, *Biophys. J.*, 1998, **74**, 2714–2721.
- N. Kaun, M. Vellekoop and B. Lendl, *Appl. Spectrosc.*, 2006, **60**, 1273–1278.
- S. Kazarian, *Anal. Bioanal. Chem.*, 2007, **388**, 529–532.
- K. Chan, X. Niu, A. de Mello and S. Kazarian, *Lab Chip*, 2010, **10**, 2170.
- J. Fagaschewski, D. Sellin, C. Wiedenhöfer, S. Bohne, H. Trieu and L. Hilterhaus, *Bioprocess Biosyst. Eng.*, 2015, **38**, 1399–1405.
- W. Walsh, A. Haller, S. van den Driesche, M. Kraft, B. Lendl and M. Vellekoop, *Biomicrofluidics*, 2012, **6**, 012803.
- P. Svasek, E. Svasek, B. Lendl and M. Vellekoop, *Sens. Actuators, A*, 2004, **115**, 591–599.
- W. Buchegger, C. Wagner, P. Svasek, B. Lendl, M. Kraft and M. Vellekoop, *Sens. Actuators, B*, 2011, **159**, 336–341.
- G. Birarda, G. Greci, L. Businaro, B. Marmioli, S. Pacor and L. Vaccari, *Microelectron. Eng.*, 2010, **87**, 806–809.
- M. Kakuta, P. Hinsmann, A. Manz and B. Lendl, *Lab Chip*, 2003, **3**, 82.
- W. Buchegger, C. Wagner, B. Lendl, M. Kraft and M. Vellekoop, *Microfluid. Nanofluid.*, 2010, **10**, 889–897.
- T. Tofteberg, M. Skolimowski, E. Andreassen and O. Geschke, *Microfluid. Nanofluid.*, 2009, **8**, 209–215.
- A. Stroock, *Science*, 2002, **295**, 647–651.
- B. Schmidt, G. Mahmud, S. Soh, S. Kim, T. Page, T. O'Halloran, B. Grzybowski and B. Hoffman, *Appl. Magn. Reson.*, 2011, **40**, 415–425.
- Y. Li, D. Zhang, X. Feng, Y. Xu and B. Liu, *Talanta*, 2012, **88**, 175–180.
- M. Gelber, M. Kole, N. Kim, N. Aluru and R. Bhargava, *Anal. Chem.*, 2017, **89**, 1716–1723.
- D. Hertzog, X. Michalet, M. Jäger, X. Kong, J. Santiago, S. Weiss and O. Bakajin, *Anal. Chem.*, 2004, **76**, 7169–7178.
- S. Yao and O. Bakajin, *Anal. Chem.*, 2007, **79**, 5753–5759.
- H. Park, S. Kim, J. Korlach, E. Rhoades, L. Kwok, W. Zipfel, M. Waxham, W. Webb and L. Pollack, *Proc. Natl. Acad. Sci. U. S. A.*, 2008, **105**, 542–547.
- K. Chan, S. Gulati, J. Edel, A. de Mello and S. Kazarian, *Lab Chip*, 2009, **9**, 2909.
- M. Nasse, M. Walsh, E. Mattson, R. Reininger, A. Kajdacsy-Balla, V. Macias, R. Bhargava and C. Hirschmugl, *Nat. Methods*, 2011, **8**, 413–416.
- R. Reddy, M. Walsh, M. Schulmerich, P. Carney and R. Bhargava, *Appl. Spectrosc.*, 2013, **67**, 93–105.
- S. Tiwari, J. Raman, V. Reddy, A. Ghetler, R. Tella, Y. Han, C. Moon, C. Hoke and R. Bhargava, *Anal. Chem.*, 2016, **88**, 10183–10190.
- S. Mittal, K. Yeh, L. Leslie, S. Kenkel, A. Kajdacsy-Balla and R. Bhargava, *Proc. Natl. Acad. Sci. U. S. A.*, 2018, **115**, E5651–E5660.
- R. Bhargava, S. Wang and J. Koenig, *Appl. Spectrosc.*, 2000, **54**, 486–495.
- A. Perro, G. Lebourdon, S. Henry, S. Lecomte, L. Servant and S. Marre, *React. Chem. Eng.*, 2016, **1**, 675–675.
- K. Chan, X. Niu, A. deMello and S. Kazarian, *Anal. Chem.*, 2011, **83**, 3606–3609.
- S. Huffman, R. Bhargava and I. Levin, *Appl. Spectrosc.*, 2002, **56**, 965–969.
- K. Chan and S. Kazarian, *Anal. Chem.*, 2012, **84**, 4052–4056.
- R. Bhargava and I. Levin, *Appl. Spectrosc.*, 2003, **57**, 357–366.
- G. Lee, C. Chang, S. Huang and R. Yang, *J. Micromech. Microeng.*, 2006, **16**, 1024–1032.
- M. Pousti, M. Joly, P. Roberge, M. Amirdehi, A. Bégin-Drolet and J. Greener, *Anal. Chem.*, 2018, **90**, 14475–14483.
- D. Kise, D. Magana, M. Reddish and R. Dyer, *Lab Chip*, 2014, **14**, 584–591.
- B. Davis, P. Carney and R. Bhargava, *Anal. Chem.*, 2010, **82**, 3474–3486.
- M. Baker, J. Trevisan, P. Bassan, R. Bhargava, H. Butler, K. Dorling, P. Fielden, S. Fogarty, N. Fullwood, K. Heys, C. Hughes, P. Lasch, P. Martin-Hirsch, B. Obinaju, G. Sockalingum, J. Sulé-Suso, R. Strong, M. Walsh, B. Wood, P. Gardner and F. Martin, *Nat. Protoc.*, 2014, **9**, 1771–1791.
- E. Kauffmann, N. Darnton, R. Austin, C. Batt and K. Gerwert, *Proc. Natl. Acad. Sci. U. S. A.*, 2001, **98**, 6646–6649.
- K. Liu, P. Gu, K. Hamaker and Z. Fan, *J. Colloid Interface Sci.*, 2012, **365**, 289–295.

- 51 B. Cortese, M. Mowlem and H. Morgan, *Sens. Actuators, B*, 2011, **160**, 1473–1480.
- 52 M. Barich and A. Krummel, *Anal. Chem.*, 2013, **85**, 10000–10003.
- 53 E. Polshin, B. Verbruggen, D. Witters, B. Sels, D. De Vos, B. Nicolai and J. Lammertyn, *Sens. Actuators, B*, 2014, **196**, 175–182.
- 54 A. Ewing, G. Clarke and S. Kazarian, *Biomicrofluidics*, 2016, **10**, 024125.
- 55 D. Guin, K. Sye, K. Dave and M. Gruebele, *Protein Sci.*, 2016, **25**, 1061–1068.
- 56 M. Jourdan and M. Searle, *Biochemistry*, 2001, **40**, 10317–10325.
- 57 A. Barth, *Biochim. Biophys. Acta, Bioenerg.*, 2007, **1767**, 1073–1101.
- 58 B. Singh, *Infrared analysis of peptides and proteins*, American Chemical Society, Washington, D.C., 2000.
- 59 Y. Yu, J. Wang, Q. Shao, J. Shi and W. Zhu, *Sci. Rep.*, 2016, **6**, 19500.
- 60 M. Kakuta, D. Jayawickrama, A. Wolters, A. Manz and J. Sweedler, *Anal. Chem.*, 2003, **75**, 956–960.
- 61 M. A. Unger, H. P. Chou, T. Thorsen, A. Scherer and S. R. Quake, *Science*, 2000, **288**, 113–116.
- 62 M. Grossman, N. Sela-Passwell and I. Sagi, *Curr. Opin. Struct. Biol.*, 2011, **21**, 678–685.
- 63 K. Maquelin, C. Kirschner, L. Choo-Smith, N. van den Braak, H. Endtz, D. Naumann and G. Puppels, *J. Microbiol. Methods*, 2002, **51**, 255–271.
- 64 K. Kuwajima, P. Kim and R. Baldwin, *Biopolymers*, 1983, **22**, 59–67.
- 65 R. Bhargava, *Appl. Spectrosc.*, 2012, **66**, 1091–1120.
- 66 B. Ivorra, J. Redondo, J. Santiago, P. Ortigosa and A. Ramos, *Phys. Fluids*, 2013, **25**, 032001.
- 67 N. Ferguson, J. Berriman, M. Petrovich, T. Sharpe, J. Finch and A. Fersht, *Proc. Natl. Acad. Sci. U. S. A.*, 2003, **100**, 9814–9819.
- 68 C. Davis and R. Dyer, *Biochemistry*, 2014, **53**, 5476–5484.
- 69 V. Andonova and P. Peneva, *Curr. Pharm. Des.*, 2018, **23**, 6630–6642.
- 70 J. Schieferstein, A. Pawate, M. Varel, S. Guha, I. Astrauskaite, R. Gennis and P. Kenis, *Lab Chip*, 2018, **18**, 944–954.